Measurement of the math xmlns="http://www.w3.org/1998/Math/MathML">mrow>mmultiscripts>mi mathvariant="normal">U/mi>mprescripts>/mprescripts>none>/none>mn>235/mn>/mmultiscripts>mo>(/mo>mi>n/mi>mo>,/mo>mi>f/mi>mo>)/mo>/mrow>/math> prompt fission neutron spectrum from 10 keV to 10 MeV induced by neutrons of energy from 1 MeV to 20 MeV

K. J. Kelly, J. A. Gomez, M. Devlin, J. M. O'Donnell, D. Neudecker, A. E. Lovell, R. C. Haight, C. Y. Wu, R. Henderson, T. Kawano, E. A. Bennett, S. M. Mosby, J. L. Ullmann, N. Fotiades, J. Henderson, T. N. Taddeucci, H. Y. Lee, P. Talou, and M. C. White

Phys. Rev. C **105**, 044615 — Published 20 April 2022

DOI: 10.1103/PhysRevC.105.044615

Measurement of the ^{235}U(n,f) Prompt Fission Neutron Spectrum from 10 keV to 10 MeV Induced by Neutrons of Energy from 1–20 MeV

K. J. Kelly[1], J. A. Gomez[1], M. Devlin[1], J. M. O'Donnell[1], D. Neudecker[1], A. E. Lovell[1], R. C. Haight[1], C. Y. Wu[2], R. Henderson[2], T. Kawano[1], E.A. Bennett[1], S. M. Mosby[1], J. L. Ullmann[1], N. Fotiades[1], J. Henderson[2], T. N. Taddeucci[1], H. Y. Lee[1], P. Talou[1], and M. C. White[1]
[1]*Los Alamos National Laboratory, Los Alamos, NM 87545, USA and*
[2]*Lawrence Livermore National Laboratory, Livermore, CA 94550, USA*
(Dated: March 30, 2022)

The characterization of fission-driven nuclear systems primarily relies on calculations of neutron-induced chain reactions, and these calculations require evaluated nuclear data as input. Calculation accuracy heavily depends on input nuclear data evaluation accuracy, and thus high precision on the experimental input to the nuclear data evaluation is essential for fundamental quantities like the energy spectrum of neutrons emitted from neutron-induced fission (i.e., the prompt fission neutron spectrum, PFNS). Despite decades of measurement efforts, prior to the measurements described in this work there were only three literature data sets for the ^{235}U(n,f) PFNS at incident neutron energies above 1.0 MeV considered reliable for inclusion in nuclear data evaluations, and no reliable data sets above 3.0 MeV incident neutron energy. In this work we report on new measurements of the ^{235}U(n,f) PFNS spanning a grid of 1.0–20.0 MeV in incident neutron energy, and 0.01–10.0 MeV in outgoing (PFNS) neutron energy. These measurements were carried out at the Weapons Neutron Research facility at the Los Alamos Neutron Science Center, and used a multi-foil parallel-plate avalanche counter target with both a Li-glass and a liquid scintillator detector array in separate experiments to span the quoted outgoing neutron energy ranges. The PFNS results are shown in terms of the energy spectra themselves as well as the average PFNS energy ($\langle E \rangle$), and ratios of $\langle E \rangle$ at forward and backward angles. The results are compared with literature data and selected nuclear data evaluations. Generally, the data agree with the ENDF/B-VIII.0 evaluation below 5.0 MeV incident neutron energy, and more closely with the JEFF-3.3 evaluation above 5.0 MeV, though no evaluations considered for comparison in this work agree with the data across all of the incident and outgoing neutron energies shown, especially in regions where the third-chance fission process becomes available. Additionally, we show a ratio of the present PFNS results for ^{235}U(n,f) with a recent and highly-correlated experiment to measure the ^{239}Pu(n,f) PFNS at the same experimental facility and with nearly identical equipment and analysis procedures. Many observations reported in this work are the first of their kind, and represent significant advancements for knowledge of the ^{235}U(n,f) PFNS.

I. INTRODUCTION

Predictions of the behavior of nuclear systems driven by neutron-induced fission rely on evaluations of the relevant nuclear physics quantities, which in turn rely on experimental data as input and to guide model predictions [1, 2]. Of particular importance in these systems is the energy spectrum of neutrons emitted promptly from neutron-induced fission, i.e., the prompt fission neutron spectrum (PFNS). The PFNS changes as a function of both the emitted, or outgoing, neutron energy, E_n^{out}, and the energy of neutron inducing the fission reaction, termed the incident neutron energy, E_n^{inc}. Owing to the complexity of the fission process, nuclear data evaluations are not sufficiently guided by measurements of the PFNS from desired nuclei at a single or a small number of E_n^{inc} values. Instead, measurements of the PFNS across a wide range of E_n^{inc} and E_n^{out} values are required. However, given the lack of literature data covering the desired E_n^{inc} and E_n^{out} ranges, nuclear data evaluators are forced to compile existing measurements at varying and limited ranges in both E_n^{inc} and E_n^{out} to extract the correct PFNS evolution and underlying model parameters.

Specifically for the ^{235}U(n,f) PFNS, only ten measurements were determined to be suitable for the ENDF/B-VIII.0 evaluation [2, 3]. Of those data sets, only the results of Knitter *et al.* [4] and Lestone *et al.* [5], both at $E_n^{inc} = 1.5$ MeV, and those of Boikov *et al.* [6] at $E_n^{inc} = 2.9$ MeV are above thermal E_n^{inc}. Rejected data sets within the E_n^{inc} range measured for this work include Condé *et al.* [7, 8] at $E_n^{inc} = 1.5$ MeV, Trufanov *et al.* [9] at $E_n^{inc} = 5.0$ MeV, Staples [10] at $E_n^{inc} = 1.5$, 2.5, and 3.5 MeV, Noda *et al.* [11] with 1 MeV bins from $E_n^{inc} = 1$–8 MeV, and Enqvist *et al.* [12] using a broad incident neutron spectrum from $E_n^{inc} = 0.5$–10.0 MeV. The data of Refs. [9–11] were rejected due to PFNS shapes appearing problematic or unphysical, while the results of Refs. [7, 8] were rejected because of insufficient uncertainty quantification and those of Ref. [12] because of the broad incident neutron energy spectrum employed. The measurement of Boikov *et al.* [6] at $E_n^{inc} = 14.7$ MeV was also rejected even though the 2.9 MeV result was included because the authors only measured at a single outgoing neutron detection angle, and thus a bias is introduced at this higher incident energy where the PFNS is believed to be far from isotropic.

In this work we report results for the measurement of the ^{235}U(n,f) PFNS over the range of $E_n^{inc} = 1$–20 MeV

and $E_n^{out} = 0.01$–10 MeV using the Weapons Neutron Research (WNR) facility at the Los Alamos Neutron Science Center (LANSCE) [13]. These measurements are part of the Chi-Nu project to measure the PFNS of major actinides at LANSCE. In an effort to maintain consistency across results from the Chi-Nu experimental effort, these ^{235}U(n,f) data were obtained using, as close as possible, the same experimental environment and analysis procedures as for the previously-published results from the Chi-Nu project on the ^{239}Pu(n,f) PFNS [14]. Thus, we frequently refer back to this highly-detailed publication for experiment and analysis details to avoid repetition. The experimental environment and details of the data acquisition are described in Sec. II, procedures for analyzing the acquired data and deriving the associated covariances of the final results are discussed in Sec. III, and the results themselves are shown in Sec. IV. The results are further broken down into ranges of E_n^{inc} with similar fission reaction mechanisms available in Secs. IV A–IV C. The average energies of the measured ^{235}U(n,f) spectra are discussed in Sec. IV D. Given the near-identical experimental procedures followed for both the ^{235}U(n,f) results shown in this work and the ^{239}Pu(n,f) results shown in Ref. [14], we also show comparisons of the PFNS results of both nuclei in Sec. IV E. Finally, conclusions are given in Sec. V.

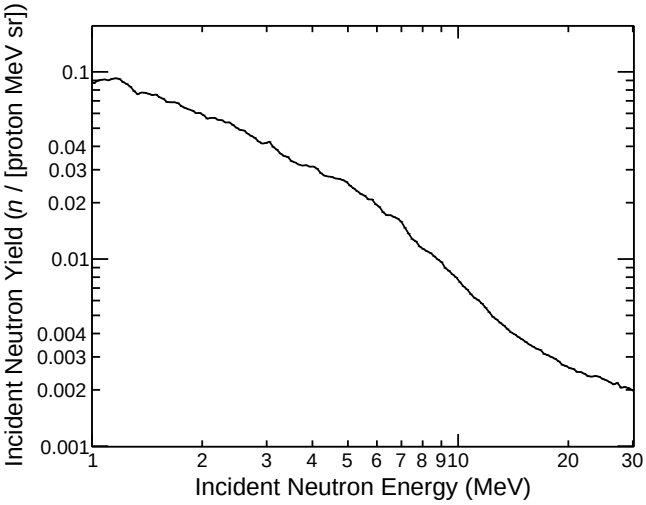

FIG. 1: The yield of incident neutrons at the Chi-Nu target position as measured with a ^{235}U flux monitor [15] placed at 19.145(15) m from the spallation target in a separate experiment. Typical proton beam current on the tungsten spallation target was ∼3.5 μA. Statistical uncertainties for this measurement range from 0.70–0.57%, which is too small to see here. Systematic uncertainties were not included as these data were not included in the analysis reported in this work.

II. EXPERIMENTAL CONFIGURATION AND ACQUIRED DATA

Incident neutrons for this experiment were provided by the LANSCE WNR facility, where a white spectrum of incident neutrons up to nearly 800 MeV is created by 800 MeV proton spallation reactions on a tungsten target. Each proton pulse is approximately 150 ps wide, and is referred to as a micropulse. The micropulses are typically separated from neighboring micropulses by ∼1.8 μs. Micropulses are also organized into groups called macropulses, each of which nominally consists of 347 micropulses, yielding a total length of approximately 625 μs for each macropulse. Finally, macropulses are typically separated from neighboring macropulses by 8.3 ms. Prior to collision of the proton beam with the tungsten target, a signal, colloquially referred to as the t_0 signal, is provided to the experimental area and used to define the incident neutron creation time. The γ rays emitted from spallation reactions are also used to ensure alignment of the t_0 signal with the spallation reaction itself. Spallation neutrons then traverse a 21.5 m flight path including a collimated beam pipe aligned to be 15° to the left of the incident proton direction before reaching the experimental area. A measured spectrum of incident neutron yield observed at this angle with respect to the incident proton beam is shown in Fig. 1.

A multi-foil parallel-plate avalanche counter (PPAC) target containing twenty electroplated deposits of approximately 5 mg each of 99.912% pure ^{235}U over a circular 4 cm diameter area, yielding roughly a 400 μg/cm^2 target thickness. Each target foil has one 5 mg deposit on each side, yielding approximately 10 mg per target foil. During operation, the PPAC was filled with continuously-flowing isobutane gas at approximately 4.2 Torr and was used to measure neutron-induced fission events on ^{235}U. Signals from the PPAC target were defined to arrive at the fission detection time, t_f, and the t_f-t_0 time difference was used to determine E_n^{inc}. The general construction and properties of these targets are described in Refs. [14, 16]. Three points are important to reiterate from Ref. [14] regarding PPAC operation: (1) the sub-nanosecond time resolution of the PPAC target was essential to facilitate of the observed precision on measurements of E_n^{inc} and E_n^{out} via time of flight, (2) PPAC detectors also measure α particles emitted from ^{235}U. The α contamination of the desired ^{235}U fission signals is a factor of ∼10^4 less than for the ^{239}Pu results of Ref. [14], and these α detections are easily accounted for with the random-coincidence background techniques described in Refs. [14, 17]. Finally, (3) the efficiency for any given fission fragment initiating an electron avalanche in the PPAC volume, thereby generating a PPAC fission signal, is dependent on the fragment emission angle and possibly, though to a much lesser extent, the fragment mass, charge, and kinetic energy. The potential systematic errors and uncertainties from item (3) were assessed using CGMF [18, 19] calculations as described in Ref. [14] and in Sec. III.

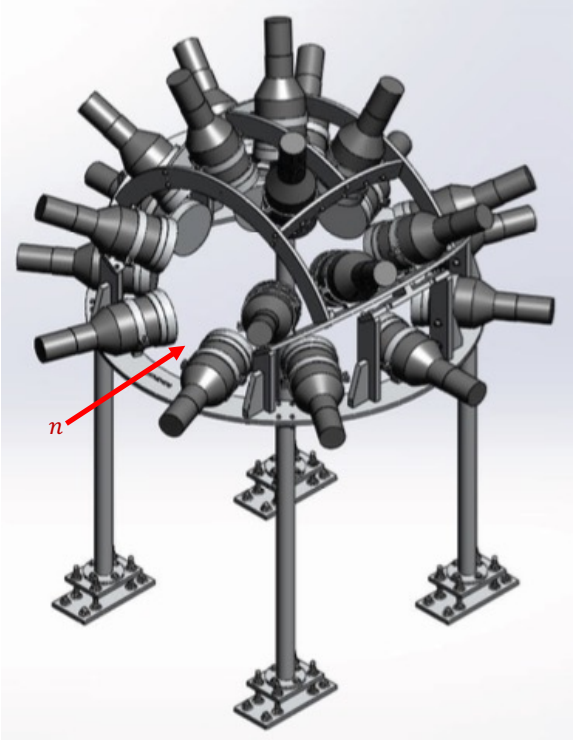

FIG. 2: A rendering of the Chi-Nu Li-glass detector array is shown. The beam enters from the lower-left of this figure, as indicated by the red arrow. The PPAC fission counter (not shown) is at the center of the array during experiments.

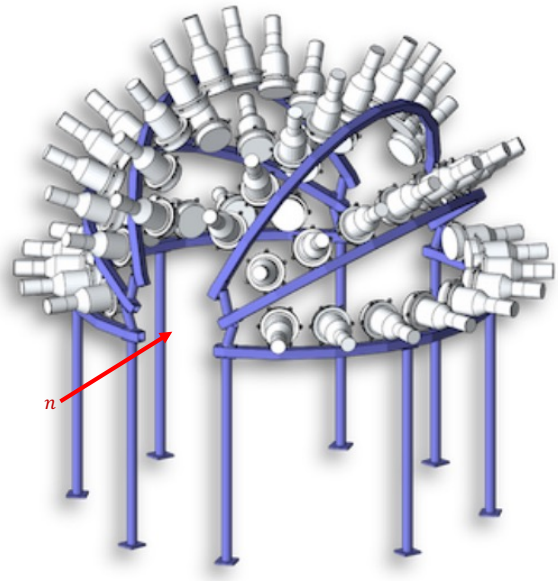

FIG. 3: A rendering of the Chi-Nu liquid scintillator detector array is shown. The beam enters from the lower-left of this figure, as indicated by the red arrow. The PPAC fission counter (not shown) is at the center of the array during experiments.

Neutrons from these measurements were detected with two unique detector arrays in separate experiments, both spanning the same E_n^{inc} range and measuring the neutron detection time, t_n. The t_n-t_f time difference yielded the inferred E_n^{out} for each measured neutron. Results for the PFNS from E_n^{out} = 0.01–1.59 MeV were extracted using a Li-glass detector array with twenty one 95% ^{6}Li-enriched GS20 Li-glass detectors and one ^{7}Li-enriched detector, all from Scintacor [20, 21], and each of which was coupled to an R1250A Hamamatsu photomultiplier tube (PMT) [22]. These detectors were held at a nominal target-to-detector-face distance of 0.400(5) m and exhibited a 1-σ time resolution of 1.03(1) ns when in coincidence with PPAC fission detections.

Results for the PFNS from E_n^{out} = 0.89–10 MeV were extracted using a liquid scintillator detector array with fifty-four 5.5 cm thick × 17.7 cm diameter cylindrical volume EJ-309 [23] detectors. Each liquid scintillator detector was coupled to an R4144 Hamamatsu PMT and held with the detector face nominally at 1.020(5) m from the target center. These detectors yielded a time resolution of 1.05(1) ns, again at 1-σ when in coincidence with PPAC fission signals. The flight path length and time resolution uncertainties are included in the results shown in this work as E_n^{out} (x axis in Secs. IV A–IV C) uncertainties, rather than uncertainties on the PFNS centroids (y axis). Renderings of the Li-glass and liquid scintillator arrays are shown in Figs. 2 and 3, respectively. High voltages for detector PMTs were supplied via a CAEN SY4527 HV supply [24]. Signals from all neutron detectors, each PPAC volume, and the t_0 timing signals were asynchronously read out with a series of 14 bit, 500 MS/s CAEN 1730B digitizers [25] using MIDAS [26, 27]. In total, the ^{235}U(n,f) Li-glass data set analyzed in this work was collected over 1074 hrs, yielding 7.05×10^8 detected fission events events, while the liquid scintillator data set was collected over 712 hrs, yielding approximately 2.70×10^8 detected fission events. The overlap region between the E_n^{out} ranges of these two detector arrays is used to combine the results from both measurements into a single PFNS result from E_n^{out} = 0.01–10 MeV as described in Refs. [14, 28] and in Sec. III.

III. ANALYSIS PROCEDURES AND COVARIANCE DETERMINATION

We briefly describe the essential processes for data reduction, background subtraction, corrections for efficiency and environmental neutron scattering, combination of the Li-glass and liquid scintillator data, corrections for incident neutron wraparound effects, and calculation of the covariance of the final results in Secs. III A, III B, III C, III D, III E, and III F, respectively. Only the necessary details are reiterated here, as identical analysis procedures have been thoroughly described in Ref. [14].

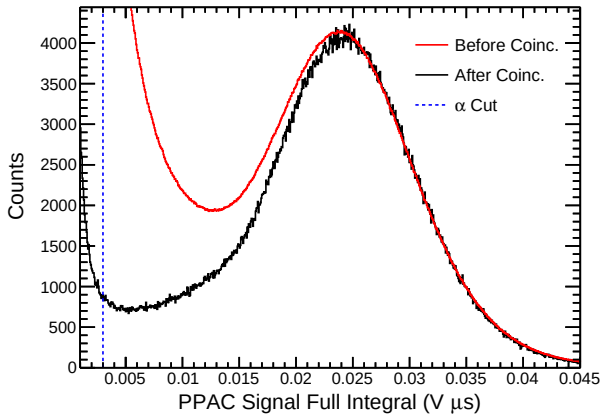

FIG. 4: (color online) An example PPAC spectrum before (red) and after (black) n-f coincidence analysis is shown. The cut placed on this spectrum is displayed as the dashed blue line. Note that the red histogram is scaled down for comparison to the black histogram.

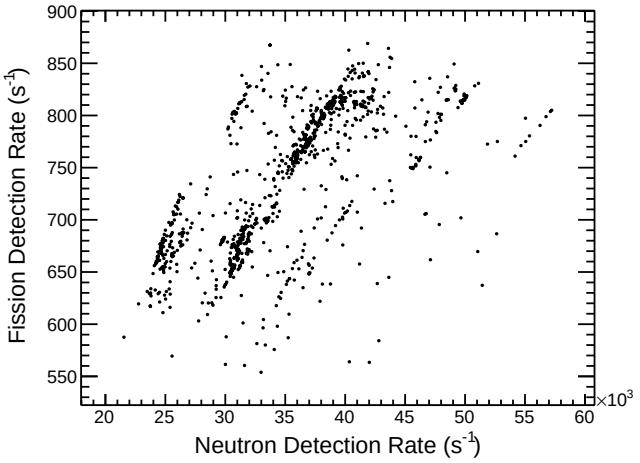

FIG. 5: A 2D graph of the total fission and neutron rates for data accepted into the final analysis of liquid scintillator data in this experiment. Each data point is summed over 1 hr of data acquisition. See the text for further details.

A. Neutron and Fission Data Reduction

Fission events in the PPAC targets have a minor overlap with spontaneous α detections in pulse integral space for this experiment. The α particles are typically detected at low pulse integrals, and the fissions at higher integrals. An example PPAC fission spectrum from this experiment is shown in red in Fig. 4. There is no clear separation between α and fission detection integrals. However, a cut is placed on the PPAC integral spectrum to cut out as many α particles as possible, while retaining as much of the detected fission signals as possible. The data accepted after this cut necessarily include some portion of the detected α particles, but as these are random detections, and therefore not in true coincidence with fission neutrons, they are easily removed with the random-coincidence background technique described in Sec. III B. Additionally, the analysis of t_n-t_f coincidences significantly reduces the contribution of α particles to the final results, as observed by the shape difference between the black and red histograms in Fig. 4. Given this reduction of α contamination, effectively 100% of the observed fission signals in coincidence with neutrons were included in the final analysis.

Neutron detections were handled uniquely for the different detector arrays because of the different physical processes and capabilities of each detector type. Li-glass detectors detect neutrons via the ^{6}Li(n,t)α reaction, which has the benefits of emitting α particles and tritons with a kinematic split of the 4.784 MeV Q-value, of having a resonance at approximately 240 keV yielding high-statistics neutron measurements near this energy, and of being a nuclear data standard cross section up through 1 MeV [3, 29]. As this is a neutron capture reaction, all neutrons are observed only once within the neutron kinematic range corresponding to the ^{6}Li(n,t)α reaction. A cut was placed as in Ref. [14] to select only neutrons detected through this reaction, which reduces the γ detections potentially identified as neutrons to a negligible level.

Neutrons are detected in liquid scintillators primarily through scattering reactions on hydrogen and carbon, with 3α-breakup reactions on carbon contributing at higher energies. Thus, a single neutron can have multiple valid detections in different detectors. This kind of effect is included in the environmental neutron response considered in Sec. III C. In addition to a kinematic selection of neutrons, with no additional Q-value energy given to the reaction products for these detections, the pulse-shape discrimination (PSD) capability of EJ-309 liquid scintillators was used to provide an additional layer of neutron selection and γ-ray rejection.

B. Random-Coincidence Backgrounds

Given the purity of the ^{235}U sample deposits, the dominant backgrounds present in the acquired data were from accidental, or random, coincidences between fission and neutron signals. These random coincidences could arise from, for example, fission neutrons in coincidence with either an α particle or a fission event that did not truly create the detected neutron, fission events in coincidence with neutrons not necessarily originating from fission, or other similar accidental coincidence scenarios. One can assume that the rates for signal detection in the fission and neutron detectors are (a) Poisson distributed in time, and (b) dominated by uncorrelated fission and neutron signals. For this scenario, the random-coincidence background rates as a function of t_n-t_f time can be calculated [14, 17, 30] from the neutron and fission data before coincidence analysis, and under the target-in-beam exper-

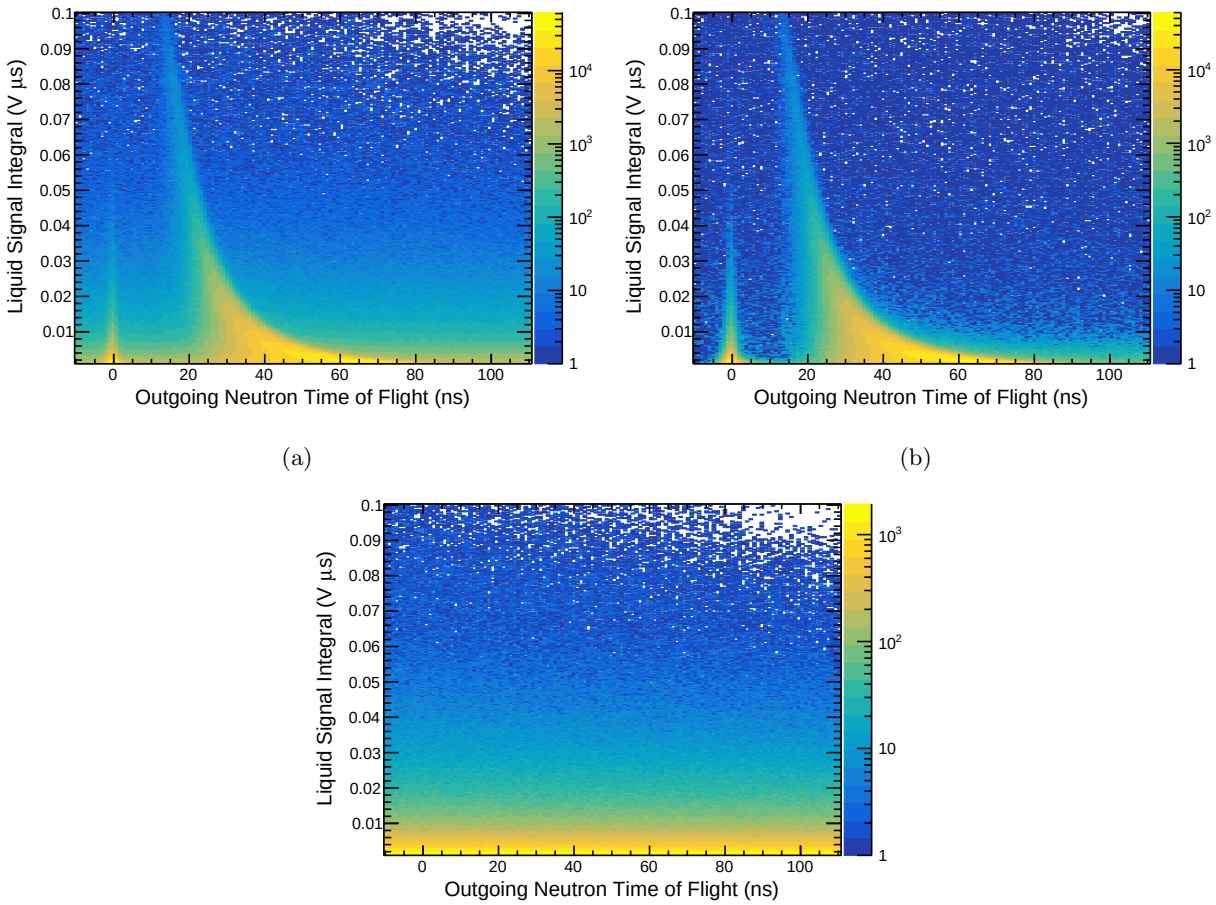

FIG. 6: (color online) Example kinematic spectrum from the liquid scintillator detector array before (a) and after (b) subtraction of data collected by shifting the PPAC signals by 1 micropulse (c) are shown here. Signals near 0 ns are the result of γ rays that survive the liquid scintillator PSD cuts. Neutrons are selected using the curved kinematic band from (15 ns, 0.1 V μs)–(80 ns, 0 V μs) on panels (a) and (b). Panel (c) shows that the primary difference between panels (a) and (b) is the reduction in random-coincidence counts surrounding this desired neutron kinematic band, distributed near unifmormly in time.

imental conditions. No additional time is required for background measurements, and no additional artificial signals are required to be included in the acquired data.

In theory, this random-coincidence background measurement method performs perfectly when the detection rates for detectors involved are either all constant, or all detection rates are constant except one [31]. However, the rates for fission and neutron detections can be influenced by incident neutron flux variations, epithermal neutron buildup within the experimental environment, long-distance neutron scatters from neighboring flight paths, and many other factors, all of which can change over the course of an experiment in a manner that appears random to the experimenter. The positive correlation between the fission and neutron rates through relation to the incident neutron beam flux can create a systematic error in the inferred random coincidence background spectrum shape and magnitude as well [31].

To mitigate these issues, accurately assign systematic uncertainties to the subtracted random-coincidence backgrounds, and obtain the correct background spectrum, two additional procedures were followed. First, the data were down-selected based on consistency of fission and neutron detection rates. A 2D graph of total fission and neutron rates for data accepted into the final analysis of liquid scintillator data is shown in Fig. 5. Each data point in Fig. 5 shows the average total fission and neutron detection rates over the course of a 1 hr segment of data acquisition. There are clear linear trends of fission and neutron signals, likely resulting from different combinations of incident neutron flux and ambient experimental conditions (see previous paragraph) demonstrating the correlations between these signals. The accepted data represent approximately 89% of the total available data.

According to the methods described in Ref. [14], the rate variations for the accepted data result in a systematic uncertainty on the random-coincidence background calculated from Ref. [17] of 1.61%. A similar analysis of the Li-glass data accepted approximately 82% of the available data and yielded a systematic uncertainty of 0.75%. The cut on Li-glass fission and neutron data rates was more strict because the low E_n^{out} values measured with this detector array naturally yield a significantly higher random-coincidence background rate.

Second, to ensure that all random-coincidence detections were removed, the data were analyzed with the PPAC and neutron detectors aligned in time, and also with the fission detection signals shifted forward and backward in time by one micropulse to provide an alternative measure of the background. The data collected with the PPAC detectors misaligned in time should be entirely background, and so any difference between the measured data and calculated random-coincidence background can be interpreted as a deficiency in the calculated background under the beam conditions of the data collected with the PPAC aligned in time. These corrections were added to the random-coincidence background, taking care to properly scale the spectra from the shifted-PPAC analyses for PPAC signals that have been shifted out of the defined coincidence windows. Examples of neutron kinematic spectra (i.e., spectra of signal integral versus outgoing neutron time of flight) from the sum over all liquid scintillator detectors before and after subtraction of the average shifted-PPAC background spectrum only are shown in Figs. 6(a) and 6(b), respectively. Figure 6(c) shows the average shifted-PPAC background specctrum itself.

As a final note on this topic, the random-coincidence background spectra determined according to Ref. [17] have extremely small statistical uncertainties compared with the true coincidence data because all pre-coincidence data are exploited, which is not the case for the spectra obtained by shifting the PPAC signals by one micropulse. Therefore, by relying on this random-coincidence background method for the majority of the background, and only relying on the shifted-PPAC data for small modifications to the background spectrum, the total statistical uncertainty of the applied background spectra is kept small enough to be only a minor contribution to the total uncertainty of the result.

C. Neutron Scattering and Efficiency Correction

Once fission-coincident neutron signals are extracted through the methods described in Secs. II, III A, and III B, final corrections must be made to transform neutron counts as a function of time, and therefore energy, as observed in the experimental environment to the correct neutron energy distribution as emitted from the target. The primary effects altering the observed PFNS shape from the true shape are environmental scattering and neutron detection efficiency. It is common for PFNS experiments to be made relative to the ^{252}Cf spontaneous fission PFNS, which is considered a standard [3, 29] (see Ref. [1] and references therein). The goal of this approach is to measure the number of neutrons at each E_n^{out} value, and then use the standard ^{252}Cf(sf) PFNS shape as the known input spectrum, also including the average number of neutrons from fission if the absolute efficiency is desired, though this is not necessary for measurements of the PFNS shape only. The ratio of the measured and known input spectra yields a correction factor relating to distortion of a PFNS from the input, and to the extent that all PFNS distributions are the same, this correction factor can be applied to measurements of the PFNS from ^{235}U(n,f) or any other spectrum.

While this approach is nearly universal among PFNS measurements, and although it seems reasonable given the general similarities across all PFNS distributions, it was shown in Ref. [32] that this method can produce significant errors for neutron-induced PFNS measurements. These errors can be particularly large in E_n^{inc} ranges where the PFNS is poorly described by a Maxwellian shape, e.g., just above onset of second- and third-chance fission and above the pre-equilibrium neutron emission threshold (see Sec. IV). Furthermore, the biases change with target nucleus identity because the PFNS shape and magnitude of these non-Maxwellian features differ with the chosen actinide.

A method for properly correcting any PFNS measurement was also demonstrated in Ref. [32], provided that the two-dimensional function of measured neutron energy via time of flight for each neutron energy upon emission from the target (i.e., the environmental detector response matrix) is known. Knowledge of the response matrix usually requires an accurate simulation of the experimental environment, but does not require any prior knowledge of the desired PFNS. However, this correction requires a measurement of the PFNS for all outgoing energies at which the PFNS exists. Given that the PFNS typically extends up through E_n^{out} = 20–30 MeV, this is difficult, and near impossible with the liquid scintillators employed for these measurements of high-energy outgoing neutrons because of the limited range of PSD validity. Alternatively, one could imagine extrapolating to higher E_n^{out} values using a Maxwellian or Watt distribution [33, 34], but these extrapolations would contain unknown systematic uncertainties since the spectrum is not guaranteed to follow either of these or any other functional forms. Also, the spectrum above the threshold for pre-equilibrium neutron emission is not close to a Maxwellian shape. Therefore, the method described in Ref. [32] was not applied to the measurements from this work.

As an alternative to following the common method of measuring relative to ^{252}Cf(sf) or applying the method described in Ref. [32], we chose to apply a correction for environmental scattering and relative neutron detection efficiency based on detailed MCNP simulations of

the experimental environment. The MCNP simulation of the Chi-Nu experiment has been discussed and validated many times in recent literature [14, 35–39]. This simulation was used to develop an average correction to the measured spectra using a distribution of PFNS shapes from ENDF/B-VIII.0 [3] and Watt spectrum parameterizations of ^{239}Pu(n,f), ^{235}U(n,f), and ^{252}Cf(sf) spectra. These various distributions result in different corrections to the measured PFNS, which (a) validates the conclusions of Ref. [32] that it is not necessarily appropriate to rely on a single reference spectrum to convert the measured data to a PFNS distribution, and (b) provides a systematic uncertainty to be applied to the resulting PFNS based on the variation in the corrections found for each of these trial distributions. This method is usually termed the "ratio-of-ratios" method [36]. The systematic uncertainty in (b) provides a notable advantage over typical measurements relative to ^{252}Cf(sf). The application of this method to the ^{235}U(n,f) data reported in this work is identical to the description given in Ref. [14], with the exception that the MCNP simulation used a ^{235}U PPAC target instead of ^{239}Pu.

D. Combination of Li-glass and Liquid Scintillator Data

Once the PFNS results for both the Li-glass and liquid scintillator data sets have been obtained by independently applying the methods described in Secs. III A–III C, all of which are described in greater mathematical detail in Ref. [14], the data from these two detector arrays were then combined to form a single PFNS result from E_n^{out} = 0.01–10 MeV. This combination procedure relies on the data points in the overlap region of these two data sets from E_n^{out} = 0.89–1.59 MeV. Specifically, the area of the Li-glass and liquid scintillator PFNS shapes are forced to be identical in this overlap region. This process could be carried out by either (a) scaling the Li-glass data to match the liquid scintillator in the overlap region, or (b) scaling the liquid scintillator data to match the Li-glass data instead. The choice of which data set is scaled initially yields different resulting covariances for the final PFNS shape. However, once the combined PFNS shape is normalized with the proper covariance propagation, as is appropriate for reporting shape results like a PFNS [28, 40], identical covariances are obtained for the final result in both (a) and (b). The mathematical derivations and demonstrations of these procedures are detailed in Refs. [14, 28].

E. Incident-Neutron Wraparound Correction

As a final correction to the PFNS results reported in this work, the "wraparound" contamination of the WNR white-source incident neutron beam was considered. Briefly, each pulse of incident neutrons at WNR reaches E_n^{inc} values down to lower than 100 keV. Given the 1.8 μs spacing of the proton bunches creating the incident neutrons via spallation reactions and the fact that the time of flight is used to define the incident neutron energy, there are multiple E_n^{inc} values that overlap in time with each other. In other words, slower neutrons from previous beam pulses can arrive at the PPAC detectors at the same time as faster neutrons from the most recent pulse. For example, incident neutrons with E_n^{inc} = 10 MeV arrive at a time of flight of t_n^{inc}(10 MeV) $\approx$ 423.8 ns, and those neutrons arrive at the same time as those with an incident energy $E_n^{inc}(t_n^{inc}[10\text{ MeV}] + 1.8\ \mu\text{s}) \approx 0.46$ MeV from the previous pulse, as well as neutrons with $E_n^{inc}(t_n^{inc}[10\text{ MeV}] + 2{\times}1.8\ \mu\text{s}) \approx 0.15$ MeV from two pulses prior, and so forth. A 0.5 in thick piece of borated polyethylene employed as a beam filter was placed at approximately 12 m from the tungsten spallation target to reduce the contribution from these wraparound neutrons in incident neutron beam. In practice it is only neutrons from one pulse prior to the most recent pulse that need to be considered.

The identity of the contaminant wraparound neutron spectrum from the micropulse prior to that of interest was approximated by a Watt spectrum fit to the E_n^{inc} = 1.0–2.0 MeV PFNS reported in this work, and the fractional contamination of the desired E_n^{inc} values by the wraparound spectrum was approximated using an exponential fit to the PPAC counts as a function of time within a macropulse [14]. Covariances of Watt and exponential fit parameters were propagated through to the final results. This contamination correction was applied to the *combined* PFNS shape, as opposed to the results from each detector individually before combination.

F. Covariance of the Final Results

Careful attention was given to covariance propagation throughout the course of this analysis, following the example of Ref. [14]. In addition to recording and propagating all covariances associated with the analysis of both the Li-glass and liquid scintillator data set, the data from these detectors are correlated to each other as well through both the data combination in the overlap region, and through the wraparound correction applied to the combined result. Furthermore, correlations are present between results at each measured E_n^{inc} range through the use of similar analysis methods. Including these cross-E_n^{inc} correlations allows for the definition of not just a series of individual covariances for each result, but the definition of a single large covariance matrix defining the correlations of all measured PFNS data points at all E_n^{inc} ranges. However, the cross-E_n^{inc} correlations do not impact the covariance of the PFNS in each individual E_n^{inc} range. The relative uncertainty on the ^{235}U(n,f) PFNS results for E_n^{inc} = 2.0–3.0 MeV from each uncertainty source determined to be non-negligible in this work is

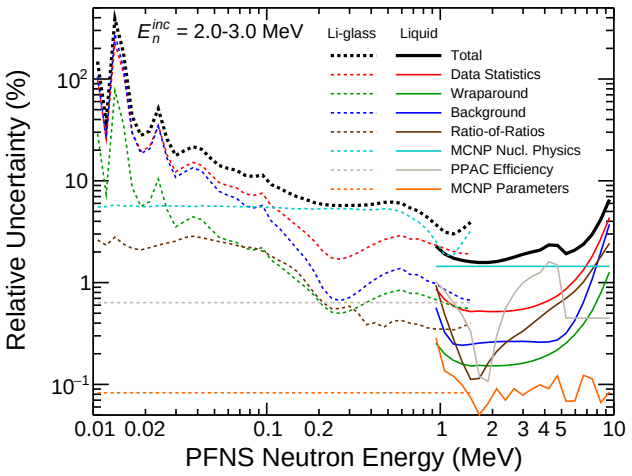

FIG. 7: (color online) The relative uncertainty from each uncertainty source determined to be non-negligible for the final PFNS result at E_n^{inc} = 2.0–3.0 MeV.

shown in Fig. 7. As E_n^{inc} increases, uncertainties from data statistics, background, and wraparound effects all increase as well since they all rely on the statistical precision of the data acquired at each E_n^{inc} bin. Other sources of uncertainty shown in Fig. 7 stay relatively constant as they are based on MCNP simulations, and are therefore effectively independent of the quality of the acquired data.

IV. RESULTS

The present ^{235}U(n,f) PFNS results are shown in Secs. IV A, IV B, and IV C for E_n^{inc} = 1.0–5.0 MeV, 5.0–10.0 MeV, and 10.0–20.0 MeV, respectively. These E_n^{inc} ranges correspond to those over which different fission reaction mechanisms are accessible [1, 39]. For example, below $E_n^{inc} \approx 5$ MeV, fission generally proceeds immediately following capture of the incident neutron, termed first-chance fission, while in the range $E_n^{inc} \approx 5.0$–10.0 MeV it is possible for the ^{236}U intermediate nucleus to either proceed directly to fission or to emit a neutron prior to the fission of a ^{235}U nucleus instead, termed second-chance fission. Above $E_n^{inc} \approx 10$ MeV in addition to first- and second-chance fission processes, two new processes also become possible: third-chance fission, in which the intermediate ^{236}U nucleus emits two neutrons prior to fission, and pre-equilibrium neutron emission preceding fission, in which the incident neutron effectively undergoes a scattering reaction with the target ^{235}U nucleus and the ^{235}U residual subsequently undergoes fission. Each of these different processes yields distinct features in the PFNS that evolve with E_n^{inc}. It is also the case that there are no reliable literature data sets available for comparison with $E_n^{inc} \gtrsim 3.0$ MeV. Thus the results shown here are the first trustworthy observations of all of these fission processes except for first-chance fission. Similar to Ref. [14], while the PFNS from E_n^{out} = 0.01-10.0 MeV for each E_n^{inc} range is included for covariance and $\langle E \rangle$ calculations, we show the PFNS distributions themselves in Secs. IV A, IV B, and IV C from E_n^{out} = 0.1–10.0 MeV as opposed to E_n^{out} = 0.01–10.0 MeV because (a) the PFNS below E_n^{out} = 100 keV typically accounts for less than 3% of the total PFNS integral, and (b) the data below E_n^{out} = 100 keV are primarily useful for confirmation of the background subtraction techniques described in Sec. III B.

It is important to note that Ref. [38] contains *preliminary*, and therefore not yet definitive, Li-glass data from the Chi-Nu experiment for E_n^{inc} = 0.7–20 MeV. Therefore, only data above E_n^{inc} = 5 MeV were used in the ENDF/B-VIII.0 evaluation [3]. The Li-glass results shown in this work were derived from the same raw data used to obtain the preliminary results in Ref. [38], though with an improved analysis as outlined in this work and in Ref. [14]. The uncertainties on the data shown in Ref. [38] are incomplete, and the data themselves are now superseded by the results shown in this work.

In addition to the PFNS results themselves, the mean energy, $\langle E \rangle$, of the PFNS as a function of E_n^{inc} and the angle-dependence of the mean energy values similar to the discussion in Ref. [39] are shown in Sec. IV D. As for the PFNS measurements above $E_n^{inc} \gtrsim 3.0$ MeV, these $\langle E \rangle$ results are the first of their kind for ^{235}U(n,f). Also, given the near-identical experimental process followed in both Ref. [14] and in this work, the high correlation between the ^{239}Pu(n,f) and ^{235}U(n,f) from the Chi-Nu experiment allows for precise measurements of the ratios of the PFNS data from these two measurements. Previously, this information was only accessible at E_n^{inc} = 1.5 MeV for two literature data sets [5, 41], one of which required corrections based on extrapolation from E_n^{inc} = 0.55 MeV, and both of which were measured with a far reduced E_n^{out} range compared with the present results (E_n^{out} = 1–10 MeV in both cases) [5, 41]. Thus, once again, all results reported for the ^{239}Pu/^{235}U PFNS ratios for $E_n^{out} < 1.0$ MeV at E_n^{inc} = 1.5 MeV shown in Sec. IV E represent first experimental observations.

Lastly, with regard to the presentation of results from the ENDF/B-VIII.0 [3], JEFF-3.3 [42], and JENDL-5.0 [43] evaluations for comparisons in this section, three points should be made clear. First, each of these evaluations has included multichance fission and pre-equilibrium neutron emission, though the precise details of how these processes are handled in each evaluation may differ. Second, while we only show uncertainties for the ENDF/B-VIII.0 library, each of these evaluations has uncertainties available. The uncertainties for the JEFF-3.3 and JENDL-5.0 libraries are comparable to those of the ENDF/B-VIII.0 evaluation, and so we only show the ENDF/B-VIII.0 uncertainties to simplify the presentation. Finally, while the JEFF-3.3 evaluation reported the PFNS on a grid of E_n^{inc} values fine enough to allow for presentation of the evaluation at the approximate

E_n^{inc} centroid for each E_n^{inc} range reported in this work, the ENDF/B-VIII.0 and JENDL-5.0 evaluations generally report the PFNS in 1 MeV E_n^{inc} increments except for regions around second-chance fission. Therefore, in order to obtain the evaluated result at the same E_n^{inc} centroid as for the JEFF-3.3 evaluation, thereby comparing each evaluation equally, the ENDF/B-VIII.0 and JENDL-5.0 evaluations were linearly interpolated as recommended by the evaluators to obtain the midpoint of each plotted E_n^{inc} range for each comparison.

A. Low Incident Energies

The present results for E_n^{inc} = 1.0–5.0 MeV are shown in Figs. 8(a)–8(d) compared with the ENDF/B-VIII.0 [3], JEFF-3.3 [42], and JENDL-5.0 [43] evaluation results at the relevant E_n^{inc} values. We reiterate that the preliminary data from Ref. [38] were *not* included in any nuclear data evaluation for this E_n^{inc} range. Figure 8(a) also shows literature data from Lestone and Shores [5] and Knitter *et al.* [4], both at E_n^{inc} = 1.5 MeV. The present results agree well within uncertainty with both experimental data sets, though the agreement within the uncertainties of Knitter *et al.* [4] is not overly surprising given the large uncertainties on those data. The present results also agree with the ENDF/B-VIII.0 and JENDL-5.0 libraries at E_n^{inc} = 1.5 MeV, but disagreements are observed with the JEFF-3.3 [42] library for the $E_n^{out} \approx$ 1.5-2.5 MeV and 3.5–7.0 MeV ranges.

Figure 8(b) shows literature data from Boikov *et al.* [6] at E_n^{inc} = 2.9 MeV, which agree well with the present results through $E_n^{out} \approx$ 4.0 MeV. A shape difference between the present results and Boikov *et al.* can be seen above $E_n^{out} \approx$ 4.0 MeV, with the present results trending closer to the nuclear data evaluations than the Boikov *et al.* data. As noted in Sec. I, the Boikov *et al.* data were collected using a single neutron-detection angle, but this feature should not yield an error in this E_n^{inc} range where the PFNS is expected to be mostly isotropic, modulo small kinematic effects. Since Boikov *et al.* did not report an efficiency for detecting fission fragments at different angles, we can only speculate that the 90° neutron-detection angle chosen may correspond to a decreased fragment detection efficiency. This kind of effect would lead to the most energetic PFNS neutrons (i.e., those emitted along the fission axis and boosted in the same direction) being detected in coincidence with fission less often, and therefore to a lower measured average PFNS energy with corresponding spectrum distortions. Assuming the fission chamber used for the Boikov *et al.* results was perpendicular to the direction of the incident neutron beam, this speculation makes sense because fragments traveling 90° with respect to the beam direction would necessarily travel within the target foil, and therefore not be detected. If this issue exists in the Boikov *et al.* data, then there would also be an issue in the efficiency for neutron detection as well, measured relative to the ^{252}Cf(sf). These errors don't directly offset each other because of neutron scattering effects in the environment [32], and so the potential net error in the Boikov *et al.* results is difficult to predict. Lastly, although the present data agree well with evaluations within their uncertainties for all E_n^{out} values in this E_n^{inc} = 2.0–3.0 MeV range, the present results show a different shape than all evaluations above $E_n^{out} \approx$ 5.0 MeV for this E_n^{inc} range.

B. Second-Chance Fission

Figure 9(a) shows the measured PFNS results at E_n^{inc} = 5.0–5.5 MeV, which is seen to be just below the onset of second-chance fission, at which point a strong enhancement of the PFNS is expected at low E_n^{out} values. Starting at E_n^{inc} = 5.5–6.0 MeV in Fig. 9(b) this feature is clearly observed in the data, and closely resembles that observed in the ENDF/B-VIII.0 and JENDL-5.0 evaluations shown. Figures 9(c) and 9(d) then demonstrate the evolution of this feature towards higher E_n^{out} values with increasing E_n^{inc}, and the predictions of all shown evaluations appear to largely match the data. The exception to this agreement is the large increase in the PFNS at high E_n^{out} values predicted by both the ENDF/B-VIII.0 and JENDL-5.0 libraries, which is not reproduced by the JEFF-3.3 library nor by the data.

Finally, the features of second-chance fission smooth out towards E_n^{inc} = 8.0–10.0 MeV in Figs. 9(e) and 9(f), with the data appearing nearly equal to a 1.32 MeV Maxwellian for E_n^{inc} = 8.0–9.0 MeV and starting to show hints of pre-equilibrium neutron emission processes at E_n^{inc} = 9.0–10.0 MeV. The observed behavior in these highest E_n^{inc} ranges in this section is broadly reproduced by the JEFF-3.3 library, but the sharp upturn of the ENDF/B-VIII.0 and JENDL-5.0 evaluations at high E_n^{out} values at these energies is still in marked disagreement with the data. We reiterate that the ENDF/B-VIII.0 library included preliminary ^{235}U(n,f) Li-glass data from Ref. [38] were included in ENDF/B-VIII.0 above E_n^{inc} = 5.0 MeV, and so agreement with this evaluation at low E_n^{out} may be expected.

C. Pre-Equilibrium Neutron Component and Third-Chance Fission

Beginning with E_n^{inc} = 10.0–11.0 and 11.0–12.0 MeV in Figs. 10(a) and 10(b) respectively, pre-equilibrium neutron emission preceding fission can be seen clearly in the evaluation trends as the presence of a peak in the PFNS at $E_n^{out} \approx$ 5–7 MeV. However, JEFF-3.3, JENDL-5.0, and the present data seem to indicate a later onset of this process indicated by a similar peak at a slightly lower E_n^{out} value and a reduced magnitude compared with ENDF/B-VIII.0. Figure 10(c) then shows the onset of third-chance fission in E_n^{inc} = 13.0 MeV ENDF/B-VIII.0 PFNS through an enhancement of the PFNS at

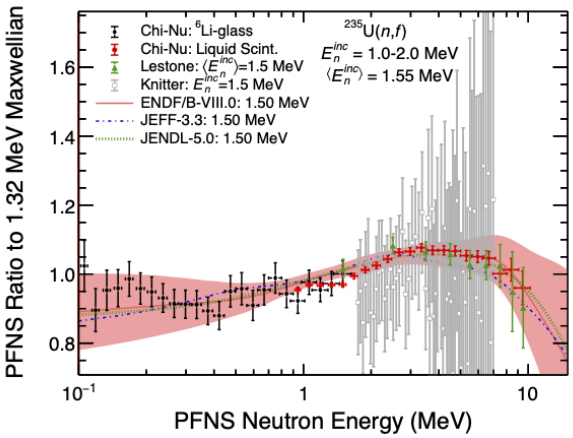

(a) (color online) The PFNS for E_n^{inc} = 1.0–2.0 MeV, corresponding to an average incident neutron energy $\langle E_n^{inc}\rangle$ = 1.55 MeV.

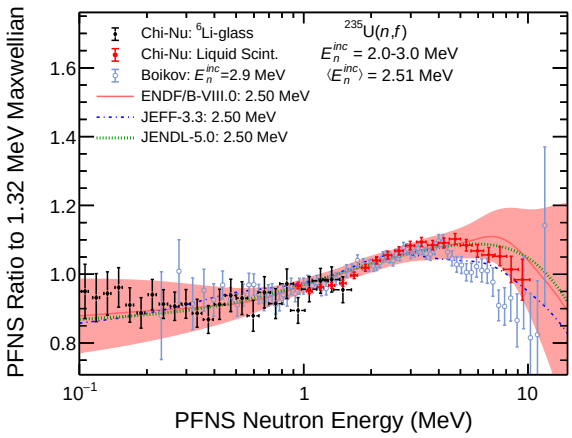

(b) (color online) The PFNS for E_n^{inc} = 2.0–3.0 MeV, corresponding to an average incident neutron energy $\langle E_n^{inc}\rangle$ = 2.51 MeV.

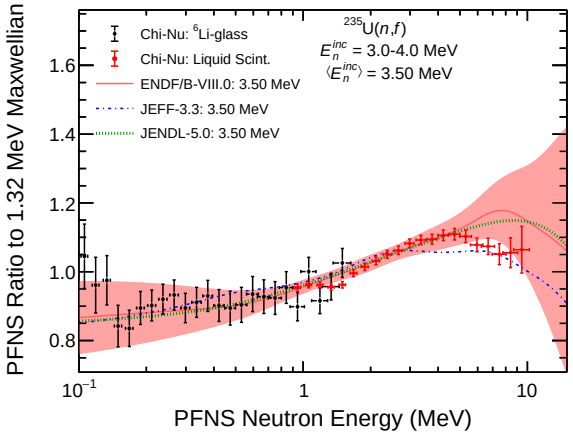

(c) (color online) The PFNS for E_n^{inc} = 3.0–4.0 MeV, corresponding to an average incident neutron energy $\langle E_n^{inc}\rangle$ = 3.50 MeV.

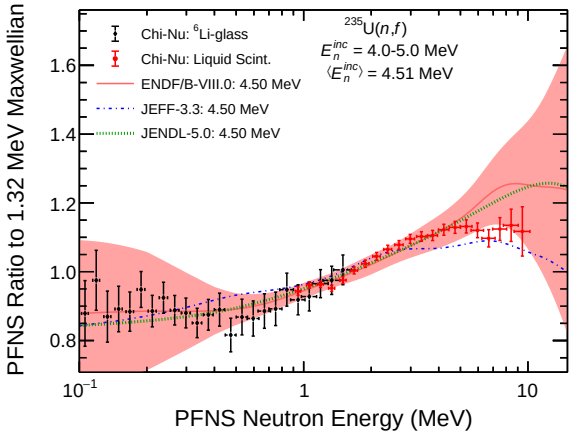

(d) (color online) The PFNS for E_n^{inc} = 4.0–5.0 MeV, corresponding to an average incident neutron energy $\langle E_n^{inc}\rangle$ = 4.51 MeV.

FIG. 8: The present PFNS results are compared here with the spectra from Lestone and Shores [5] and Knitter *et al.* [4], both at E_n^{inc} = 1.5 MeV, as well as with data from Boikov *et al.* [6] at E_n^{inc} = 2.9 MeV. Spectra from the ENDF/B-VIII.0 [3], JEFF-3.3 [42], and JENDL-5.0 [43] evaluations at the relevant E_n^{inc} values are shown as the solid red, dashed blue, and dotted green lines, respectively. The shaded region surrounding the ENDF/B-VIII.0 curve represents 1-σ uncertainty. Note that the evaluation spectra are evaluated at a single E_n^{inc} value and the other experimental spectra are integrated over different E_n^{inc} ranges.

low E_n^{out} values, similar to that observed at the onset of second-chance fission, but both the results presented here and the JEFF-3.3 evaluation seem to predict a less pronounced onset of this fission process. This also appears true for E_n^{inc} = 13.0–14.0 and 14.0–15.0 MeV in Figs. 10(d) and 10(e). The position and magnitude of the pre-equilibrium neutron peak observed in the present results appear to be near identical to that predicted by JEFF-3.3 for E_n^{inc} = 12.0–14.0 MeV, with some discrepancies present for E_n^{inc} = 14.0–15.0 MeV.

Above E_n^{inc} = 15.0 MeV in Figs. 11(a)–11(e) the present results again largely agree with the JEFF-3.3 evaluation library. The ENDF/B-VIII.0 evaluation appears to predict a reduction in the PFNS compared with the data at $E_n^{out} \approx$ 1.5–4.0 MeV for much of the E_n^{inc} = 15.0–20.0 MeV range spanned by these figures, while the JEFF-3.3 library appears to generally agree with the shape of the data and the JENDL-5.0 library is in slightly worse agreement with the data than JEFF-3.3. The higher relative contribution of the PFNS above $E_n^{out} \approx$ 5.0 MeV in ENDF/B-VIII.0 and JENDL-5.0 also continues through these incident neutron energies with JENDL-5.0 exceeding ENDF/B-VIII.0 for much of this E_n^{inc} range and is not well reproduced by the data, though near E_n^{inc} = 18.0–20.0 MeV this difference becomes less obvious.

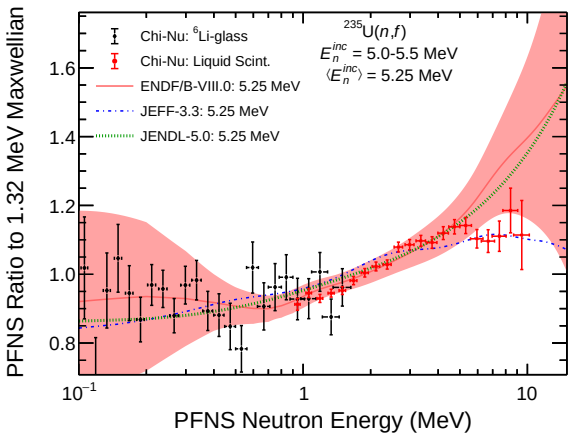

(a) (color online) The PFNS for E_n^{inc} = 5.0–5.5 MeV, corresponding to an average incident neutron energy $\langle E_n^{inc} \rangle$ = 5.25 MeV.

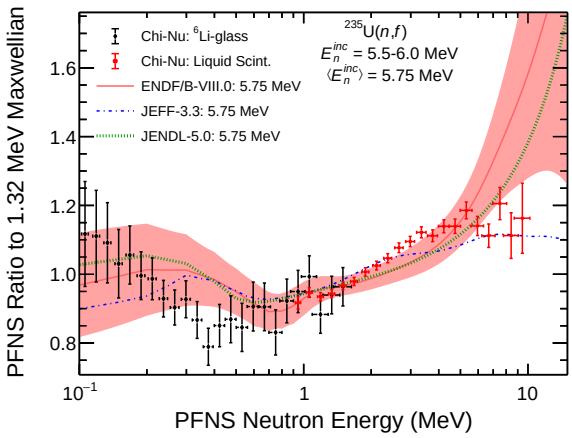

(b) (color online) The PFNS for E_n^{inc} = 5.5–6.0 MeV, corresponding to an average incident neutron energy $\langle E_n^{inc} \rangle$ = 5.75 MeV.

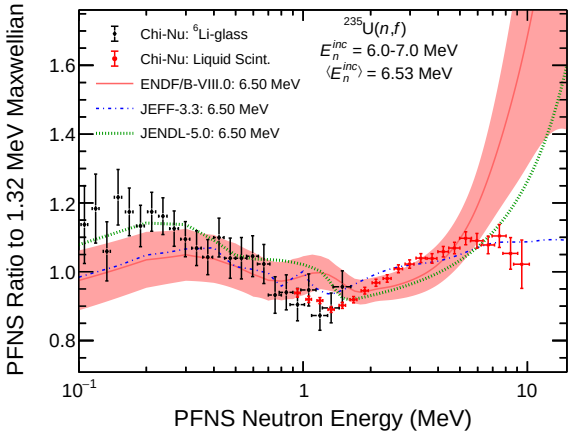

(c) (color online) The PFNS for E_n^{inc} = 6.0–7.0 MeV, corresponding to an average incident neutron energy $\langle E_n^{inc} \rangle$ = 6.53 MeV.

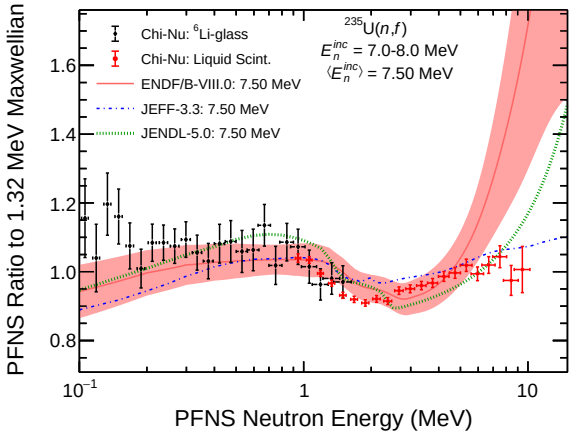

(d) (color online) The PFNS for E_n^{inc} = 7.0–8.0 MeV, corresponding to an average incident neutron energy $\langle E_n^{inc} \rangle$ = 7.50 MeV.

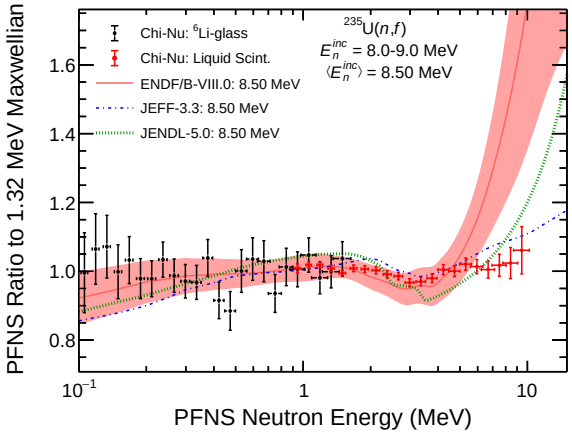

(e) (color online) The PFNS for E_n^{inc} = 8.0–9.0 MeV, corresponding to an average incident neutron energy $\langle E_n^{inc} \rangle$ = 8.50 MeV.

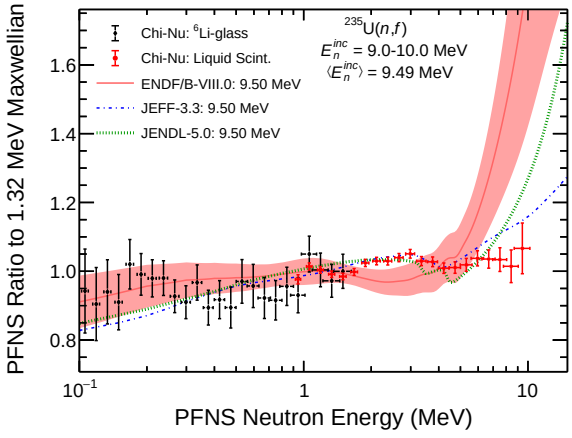

(f) (color online) The PFNS for E_n^{inc} = 9.0–10.0 MeV, corresponding to an average incident neutron energy $\langle E_n^{inc} \rangle$ = 9.49 MeV.

FIG. 9: The present PFNS results are compared here with the ENDF/B-VIII.0 [3], JEFF-3.3 [42], and JENDL-5.0 [43] evaluations, shown respectively as solid red, dashed blue, and dotted green lines, for E_n^{inc} ranges corresponding to a combination of first- and second-chance fission. The shaded region surrounding the ENDF/B-VIII.0 curve represents 1-σ uncertainty. Note that the evaluation spectra are evaluated at a single E_n^{inc} value and the other experimental spectra are integrated over different E_n^{inc} ranges.

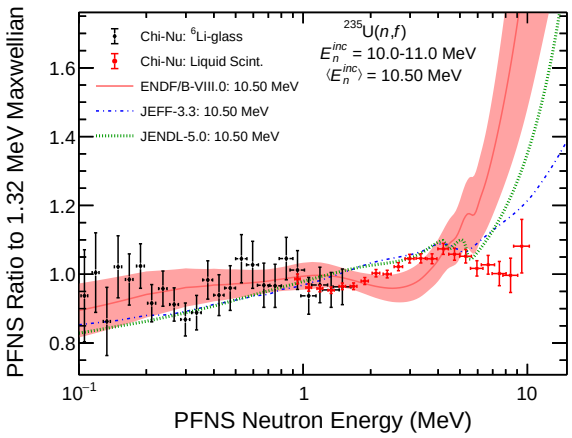

(a) (color online) The PFNS for E_n^{inc} = 10.0–11.0 MeV, corresponding to an average incident neutron energy $\langle E_n^{inc} \rangle$ = 10.50 MeV.

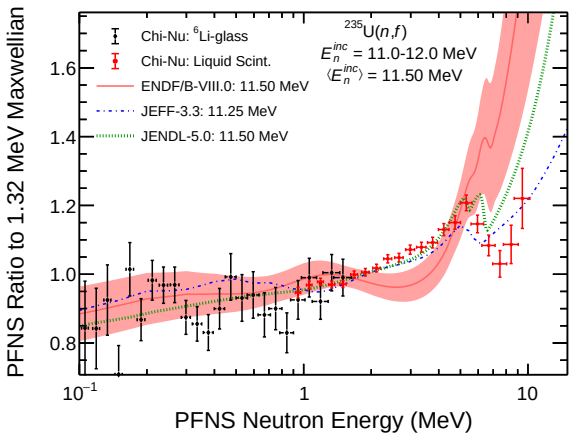

(b) (color online) The PFNS for E_n^{inc} = 11.0–12.0 MeV, corresponding to an average incident neutron energy $\langle E_n^{inc} \rangle$ = 11.50 MeV.

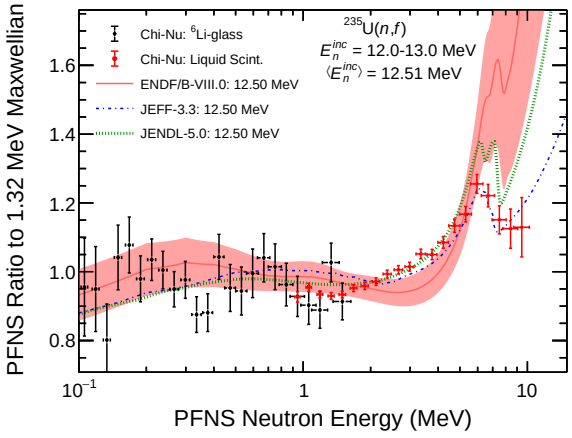

(c) (color online) The PFNS for E_n^{inc} = 12.0–13.0 MeV, corresponding to an average incident neutron energy $\langle E_n^{inc} \rangle$ = 12.51 MeV.

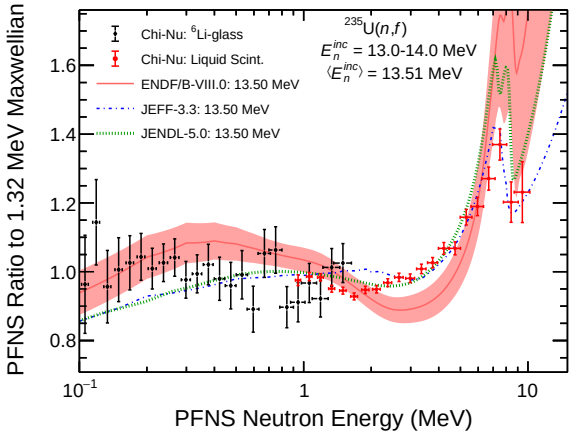

(d) (color online) The PFNS for E_n^{inc} = 13.0–14.0 MeV, corresponding to an average incident neutron energy $\langle E_n^{inc} \rangle$ = 13.51 MeV.

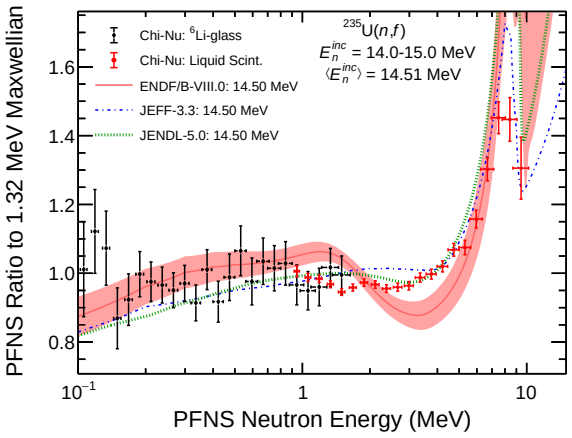

(e) (color online) The PFNS for E_n^{inc} = 14.0–15.0 MeV, corresponding to an average incident neutron energy $\langle E_n^{inc} \rangle$ = 14.51 MeV.

FIG. 10: The present PFNS results are compared here with the ENDF/B-VIII.0 [3], JEFF-3.3 [42], and JENDL-5.0 [43] evaluations, shown respectively as solid red, dashed blue, and dotted green lines, for E_n^{inc} ranges corresponding to a combination of first-, second-, and third-chance fission as well as pre-equilibrium neutron emission preceding fission from E_n^{inc} = 10–15 MeV. The shaded region surrounding the ENDF/B-VIII.0 curve represents 1-σ uncertainty. Note that the evaluation spectra are evaluated at a single E_n^{inc} value and the other experiment spectra are integrated over different E_n^{inc} ranges.

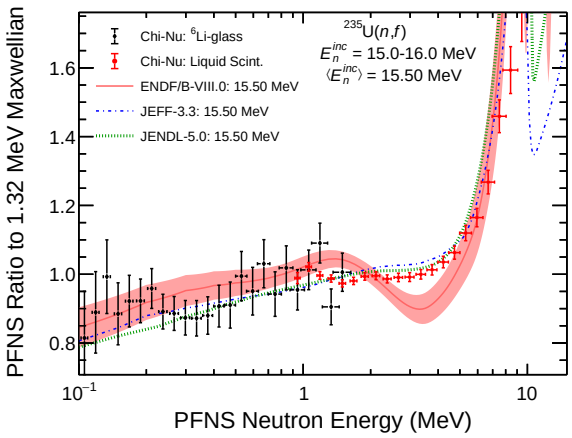

(a) (color online) The PFNS for E_n^{inc} = 15.0–16.0 MeV, corresponding to an average incident neutron energy $\langle E_n^{inc} \rangle$ = 15.50 MeV.

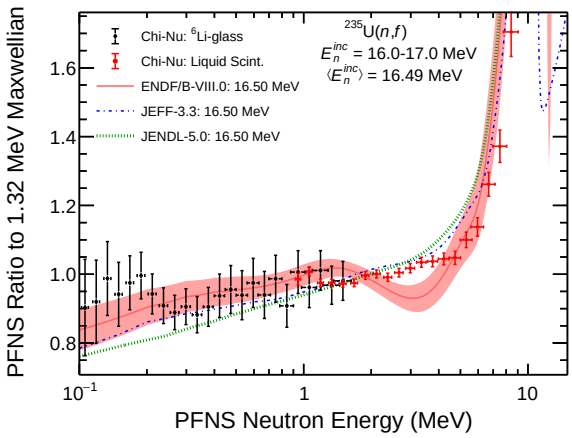

(b) (color online) The PFNS for E_n^{inc} = 16.0–17.0 MeV, corresponding to an average incident neutron energy $\langle E_n^{inc} \rangle$ = 16.49 MeV.

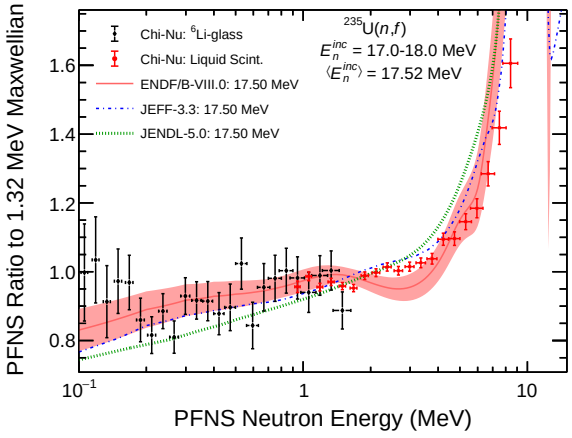

(c) (color online) The PFNS for E_n^{inc} = 17.0–18.0 MeV, corresponding to an average incident neutron energy $\langle E_n^{inc} \rangle$ = 17.52 MeV.

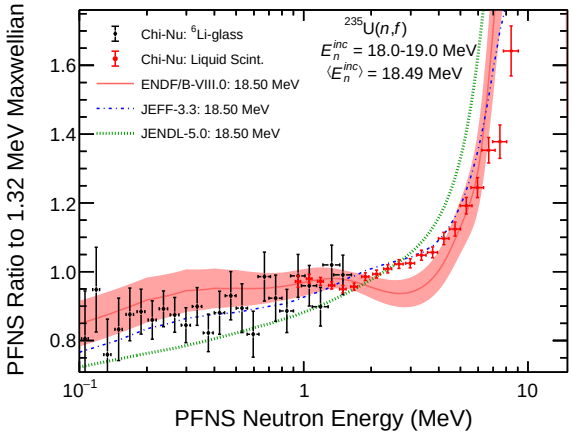

(d) (color online) The PFNS for E_n^{inc} = 18.0–19.0 MeV, corresponding to an average incident neutron energy $\langle E_n^{inc} \rangle$ = 18.49 MeV.

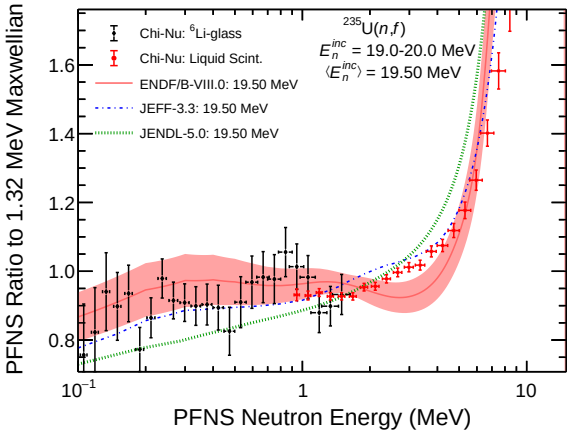

(e) (color online) The PFNS for E_n^{inc} = 19.0–20.0 MeV, corresponding to an average incident neutron energy $\langle E_n^{inc} \rangle$ = 19.50 MeV.

FIG. 11: The present PFNS results are compared here with the ENDF/B-VIII.0 [3], JEFF-3.3 [42], and JENDL-5.0 [43] evaluations, shown respectively as solid red, dashed blue, and dotted green lines, for E_n^{inc} ranges corresponding to a combination of first-, second-, and third-chance fission as well as pre-equilibrium neutron emission preceding fission from E_n^{inc} = 15–20.0 MeV. The shaded region surrounding the ENDF/B-VIII.0 curve represents 1-σ uncertainty. Note that the evaluation spectra are evaluated at a single E_n^{inc} value and the other experiment spectra are integrated over different E_n^{inc} ranges.

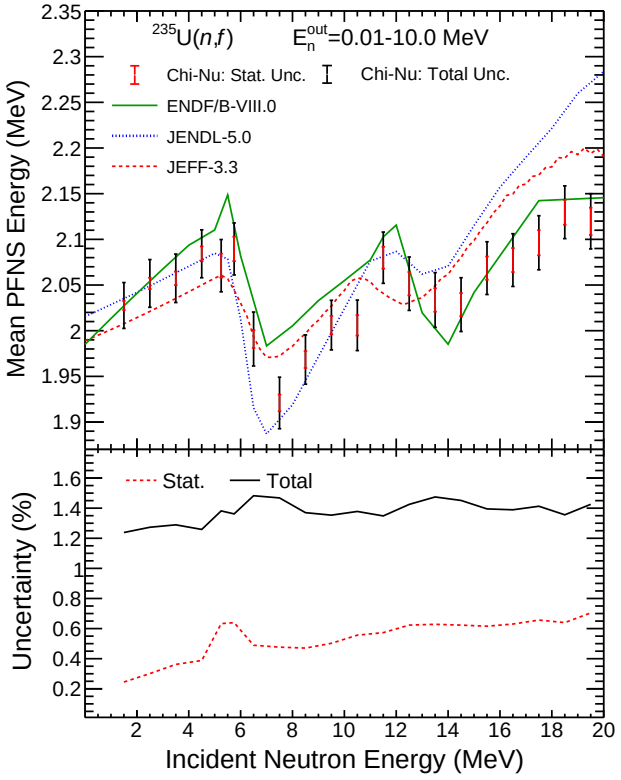

FIG. 12: (color online) (Top) The $\langle E \rangle$ values calculated from the present PFNS results are shown as the black and red errors bars, indicating total and statistical uncertainties, respectively. The ENDF/B-VIII.0, JEFF-3.3, and JENDL-5.0 evaluation library results are shown as the solid green, dashed red, and dotted blue lines, respectively, for comparison. (Bottom) The total and statistical uncertainties of the $\langle E \rangle$ calculated from the present results are shown as the solid black and dashed red lines.

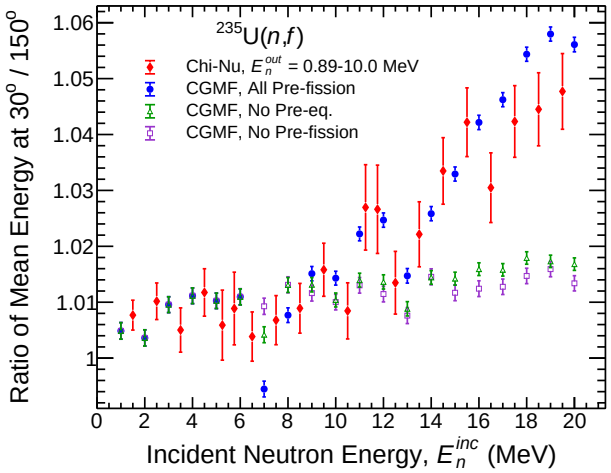

FIG. 13: (color online) The ratio of $\langle E \rangle$ measured with the liquid scintillator detector array at a neutron-detection angle of 30° to that at 150° is shown here in red, compared to results calculated using the CGMF [18, 19] code. Calculated CGMF results with no pre-fission neutrons, all pre-fission neutrons except pre-equilibrium neutrons emitted prior to fission, and all pre-fission neutrons are shown as the open violet squares, open green triangles, and full blue circles, respectively.

Lastly, it is generally true that no single evaluation agrees with the data throughout the E_n^{inc} ranges discussed in this section. This is not entirely surprising since there is a lack of data to guide evaluations, and thus evaluations are extrapolating in these ranges, to an extent. While a detailed comparison of evaluation methodology and potential sources of disagreement with the data is beyond the scope of this work, the most likely sources of error may to be the height and strength of multichance fission barriers, details of the pre-equilibrium component of the PFNS, and potentially a lack of reliable fission fragment yields as a function of E_n^{inc}.

D. Mean PFNS Energies

The average E_n^{out} of a PFNS, $\langle E \rangle$, is calculated as the E_n^{out}-weighted average of the PFNS [14]. This quantity, calculated over the range E_n^{out} = 0.01–10.0 MeV for each E_n^{inc} range shown in Secs. IV A, IV B, and IV C, is given as a function of incident energy in the top panel of Fig. 12. The total and statistical uncertainties on the calculated $\langle E \rangle$ values are shown as black and red uncertainties, respectively. Evaluated results from the ENDF/B-VIII.0, JEFF-3.3, and JENDL-5.0 [43] libraries are shown as well. The bottom panel of Fig. 12 shows the relative total and statistical uncertainties of the $\langle E \rangle$ values calculated from the present results.

Below E_n^{inc} = 12 MeV, the present results appear to agree best with the JENDL-5.0 library. The $\langle E \rangle$ slope from E_n^{inc} = 1–5 MeV is nearly identical for both the JEFF-3.3 and JENDL-5.0 libraries, and this slope seems to agree with that of the data as does the overall magnitude of the JENDL-5.0 library in this range, though the ENDF/B-VIII.0 library predicts a steep slope in this E_n^{inc} range that is at odds with the data and other plotted evaluations. Each plotted evaluation seems to predict roughly the same threshold for second-chance fission, represented in $\langle E \rangle$ as a sharp drop in value. The magnitude of this "second-chance-fission dip" appears to broadly agree best with the ENDF/B-VIII.0 and JENDL-5.0 libraries, though JENDL-5.0 displays an $\langle E \rangle$ drop that is too sharp compared with the data. Conversely, the JEFF-3.3 library shows a second-chance-fission dip that is too shallow compared with the data. From E_n^{inc} = 8–12 MeV, the upward slope of the JENDL-5.0 library agrees best with the data. As a final point on this E_n^{inc} range, it is worth noting that the E_n^{inc} = 10–11 MeV

point in the data appears low compared with the upward $\langle E \rangle$ slope of the surrounding data points. This subtle feature of the calculated $\langle E \rangle$ values will be revisited in this section.

The threshold for third-chance fission, represented in $\langle E \rangle$ as another decrease in value near $E_n^{inc} = 11$ MeV in the data, does not agree with any plotted evaluation in threshold position, magnitude, or shape of $\langle E \rangle$ decrease. The JEFF-3.3 library appears to predict the threshold for third-chance fission significantly lower in E_n^{inc} than in the data, and with an $\langle E \rangle$ decrease that is again too shallow. The JENDL-5.0 library may have the best match with the data in terms of threshold for third-chance fission, but the magnitude of this decrease in $\langle E \rangle$ is too small. The ENDF/B-VIII.0 library appears to have employed a threshold for third-chance that is slightly too high in E_n^{inc}, and is the only plotted library that appears to overpredict the magnitude of the $\langle E \rangle$ drop compared with the data. Finally, the ENDF/B-VIII.0 library provides the best agreement for $\langle E \rangle$ evolution from $E_n^{inc} = 15$–20 MeV, though the $\langle E \rangle$ shape of JEFF-3.3 above $E_n^{inc} = 15$ MeV also appears very similar to the data.

Similar to the analysis presented in Ref. [39], we also show the $\langle E \rangle$ ratio for data obtained at a neutron-detection angle of $30^o \pm 5^o$ to that of $150^o \pm 5^o$ for the liquid scintillator results shown in this work in Fig. 13. The data in Fig. 13 include full covariance propagation. Since there are no nuclear data evaluations that currently provide an angle-dependent PFNS, we instead compare to calculations with the CGMF [18, 19, 44] code, considering only neutrons emitted within the angular range of 30^o and $150^o \pm 5^o$. The emitted neutron energies from CGMF are not broadened to match the resolution of the data.

As would be expected based on the forward-peaked anisotropy of pre-equilibrium neutrons emitted prior to fission, once the threshold for this reaction mechanism is crossed the ratio $30^o/150^o$ $\langle E \rangle$ ratio increases sharply in the data. However, at $E_n^{inc} \approx 16$ MeV the pre-equilibrium neutron component of the PFNS, which looks like a peak when divided by the Maxwellian, begins to extend beyond the maximum $E_n^{out} = 10$ MeV covered in this work, yielding a downwards stagger in the $\langle E \rangle$ ratio near this E_n^{inc} value. Since the emitted neutron energies in CGMF are not broadened to match the data, this decrease in CGMF is not seen until a higher E_n^{inc}. To lend validity to the assertion that this forward-peaked anisotropy is due to the pre-equilibrium process, the CGMF calculations were analyzed to include (1) no pre-fission neutrons, (2) all pre-fission neutrons except those emitted via the pre-equilibrium process, and (3) all pre-fission neutrons. The sharp increase in $\langle E \rangle$ ratio is not seen in analyses (1) or (2) of the CGMF calculation results, and is only present when pre-equilibrium pre-fission neutrons are included in the calculation. Lastly, we note that this $\langle E \rangle$ ratio displays an increase relative to neighboring E_n^{inc} ranges in the $E_n^{inc} = 11$–12 MeV range.

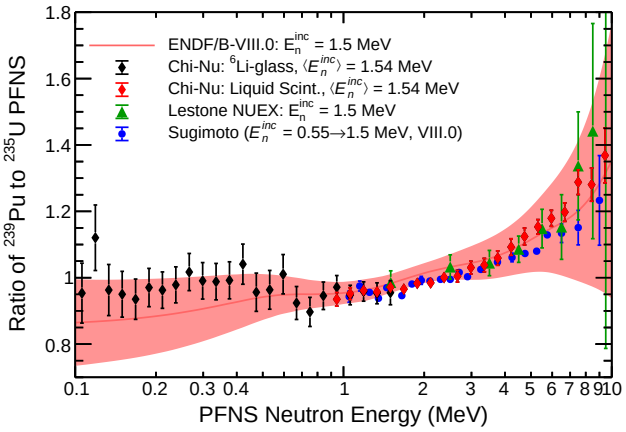

FIG. 14: (color online) The ratio of the ^{239}Pu(n,f) PFNS results from Ref. [14] to the present ^{235}U(n,f) results, both at $E_n^{inc} = 1.0$–2.0 MeV, are shown as the black and red diamonds for Li-glass and liquid scintillator data, respectively.. The ENDF/B-VIII.0 evaluation results are shown as solid red line with the shaded region displaying the evaluated uncertainty. Data from Lestone *et al.* [5] are shown as the green triangles, and those of Sugimoto *et al.* [41] are shown as the blue circles.

Furthermore, this increase is reproduced by the CGMF calculations, but was not observed in the ^{239}Pu(n,f) results of Refs. [14, 39], and also coincides with a decrease the $\langle E \rangle$ value in the same E_n^{inc} range shown in Fig. 12. This subtle feature of the $\langle E \rangle$ of the reported results is currently being investigated further.

E. Comparisons of Chi-Nu PFNS Results for ^{235}U(n,f) and ^{239}Pu(n,f)

As a final results topic, we present the ratio of the ^{239}Pu(n,f) PFNS of Ref. [14] to the ^{235}U(n,f) PFNS presented in this work. The PFNS results from these two experiments are highly correlated in that the data for both measurements were collected in effectively the same experimental environment with the exception of the change in target nucleus identity in the near-identical PPAC chambers used for both experiments. The same analysis techniques were applied for the analysis of both measurements. As such, propagation of covariances to the ^{239}Pu/^{235}U PFNS ratio reduces all uncertainties besides statistical uncertainties to a negligible level.

In Fig. 14 we show data for the ^{239}Pu/^{235}U PFNS ratio for $E_n^{inc} = 1.0$–2.0 MeV. This is the only incident energy range for which there are other experimental measurements available for comparison. Specifically, the data of Lestone *et al.* [5] are available at an average $E_n^{inc} = 1.5$ MeV and the results of Sugimoto *et al.* [41], while originally measured at $E_n^{inc} = 0.55$ MeV, were modified to $E_n^{inc} = 1.5$ MeV according to the ENDF/B-VIII.0

library, though neither of these data sets extends below $E_n^{out} = 1.0$ MeV, making the results reported here a significant improvement on previously available data. We also compare to the ENDF/B-VIII.0 library for reference. The present data agree within uncertainties with Lestone and ENDF/B-VIII.0 for all E_n^{out}, and also with Sugimoto until approximately $E_n^{out} = 5$ MeV though the general trend observed by Sugimoto *et al.* is broadly reproduced at higher energies by the present results. Results for the ^{239}Pu/^{235}U PFNS ratio are available for additional E_n^{inc} ranges, though these results will be discussed in a future publication.

V. CONCLUSIONS

The PFNS is a fundamental quantity for reliable calculations of reactive systems driven by neutron-induced fission. However, after decades of measurement attempts, accurate measurements of the PFNS for wide ranges of E_n^{inc} and E_n^{out} are still needed to achieve the desired accuracy in nuclear data evaluations. Specifically for the ^{235}U(n,f) PFNS, only three reliable literature data sets in the range of E_n^{inc} =1.0–3.0 MeV exist, and no reliable data exist above $E_n^{inc} = 3.0$ MeV.

We report in this work a measurement of the ^{235}U(n,f) PFNS for twenty E_n^{inc} ranges from $E_n^{inc} = 1.0$–20.0 MeV and sixty-five data E_n^{out} data points from $E_n^{out} = 0.01$–10.0 MeV for each E_n^{inc} range. These measurements used two unique neutron detector arrays to measure low- and high-E_n^{out} ranges of the PFNS in separate experiments, both using the same experimental area and fission target. Thorough covariance calculations were carried out for all data shown in this work, identically following the procedures described in Ref. [14]. The second- and third-chance fission processes are clearly observed in the average PFNS energies and the spectral shapes as well as the pre-equilibrium neutron emission process preceding fission. Agreement with available nuclear data evaluations varies depending on the E_n^{inc} studied. Below $E_n^{inc} = 5$ MeV, the ENDF/B-VIII.0 evaluation seems to best reproduce the PFNS results, though above this E_n^{inc} range the JEFF-3.3 evaluation largely agrees with the data, especially for high-E_n^{out} values where the ENDF/B-VIII.0 evaluation trends notably higher than the data. The threshold for second-chance fission in evaluations appears to agree with the data and the pre-equilibrium neutron emission component of the PFNS in the JEFF-3.3 evaluation agrees well with the data, but the third-chance fission features in the data do not agree well with any known evaluation.

The conclusions regarding the PFNS distributions are effectively the same as for the $\langle E \rangle$ values. Additionally, we show the ratio of $\langle E \rangle$ values calculated at neutron-detection angles of 30^o and 150^o, comparing with calculation results from the CGMF code. The data agree well with results from this code, including an increase in the ratio observed at approximately the threshold for third-chance fission. Finally, given the high correlation between this ^{235}U(n,f) experiment and a previous ^{239}Pu(n,f) PFNS experiment carried out in the same experimental facility and by the same experimental team, we also show results for the ^{239}Pu/^{235}U PFNS ratio for $E_n^{inc} = 1.0$–2.0 MeV. This PFNS ratio extends well below any previous measurements at this E_n^{inc} range, and largely agrees with available data. Many of the results shown in this work represent first reliable experimental observations of important features of the ^{235}U(n,f) PFNS, if not first ever observations, and the results shown in this work represent significant improvements on the sparse literature data for the ^{235}U(n,f) PFNS.

VI. ACKNOWLEDGEMENTS

This work was supported by the U.S. Department of Energy through Los Alamos National Laboratory. and Lawrence Livermore National Laboratory. Los Alamos National Laboratory is operated by Triad National Security, LLC, for the National Nuclear Security Administration of the U.S. Department of Energy (Contract No. 89233218CNA000001). Work at Lawrence Livermore National Laboratory was performed under Contract No. DE-AC52-07NA27344. We would like to thank F. David Sattler for design work on the Chi-Nu arrays and Mark Chadwick for guidance and discussions. We would also like to acknowledge the contributions of B. Bucher, B. Perdue, T. Bredeweg, M.B. Chadwick., A. Chyzh, E. Kwan, S. Wender, G. Rusev, M. Jandel, S. Sjue, M. E. Rising, C. J. Solomon, I. Stetcu, and J. Lestone to the Chi-Nu project.

[1] R. Capote, Y.-J. Chen, F.-J. Hambsch, N. V. Kornilov, J. P. Lestone, *et al.*, Nucl. Data Sheets **131**, 1 (2016).
[2] D. Neudecker, P. Talou, T. Kawano, A. Kahler, M. White, *et al.*, Nucl. Data Sheets **148**, 293 (2018).
[3] D. A. Brown, M. B. Chadwick, R. Capote, A. C. Kahler, A. Trkov, *et al.*, Nucl. Data Sheets **148**, 1 (2018).
[4] H.-H. Knitter, M. M. Islam, and M. Coppola, Z. Phys. **257**, 108 (1972).
[5] J. P. Lestone and E. F. Shores, Nucl. Data Sheets **119**, 213 (2014).
[6] G. Boykov, V. Dmitriev, G. Kudyaev, Y. Ostapenko, M. Svirin, *et al.*, Sov. J. Nucl. Phys. **257**, 108 (2014).
[7] H. Condé and G. During, Arkiv für Fysik **29**, 307 (1965).
[8] H. Condé and G. During, Arkiv für Fysik **29**, 313 (1965).
[9] A. M. Trufanov, G. N. Lovchikova, G. N. Smirenkin, A. V. Polyakov, and V. A. Vinogradov, Phys. Atomic Nucl. **57**, 572 (1994).

[10] P. A. Staples, *Prompt Fission Neutron Energy Spectra Induced by Fast Neutrons*, Ph.D. thesis, University of Massachusetts Lowell (1993).

[11] S. Noda, R. C. Haight, R. O. Nelson, M. Devlin, J. M. O'Donnell, *et al.*, Phys. Rev. C **83**, 034604 (2011).

[12] A. Enqvist, B. M. Wieger, L. Huang, M. Flaska, S. A. Pozzi, *et al.*, Phys. Rev. C **86**, 064605 (2012).

[13] P. W. Lisowski and K. F. Schoenberg, Nucl. Instrum. Methods A **562**, 910 (2006).

[14] K. J. Kelly, M. Devlin, J. M. O'Donnell, J. A. Gomez, D. Neudecker, *et al.*, Phys. Rev. C **102**, 034615 (2020).

[15] S. A. Wender, S. Balestrini, A. Brown, R. C. Haight, C. M. Laymon, *et al.*, Nucl. Instrum. Methods A **336**, 226 (1993).

[16] C. Y. Wu, R. A. Henderson, R. C. Haight, H. Y. Lee, T. N. Taddeucci, *et al.*, Nucl. Instrum. and Methods A **794**, 76 (2015).

[17] J. M. O'Donnell, Nucl. Instrum. Methods A **805**, 87 (2016).

[18] P. Talou, R. Vogt, J. Randrup, M. E. Rising, S. A. Pozzi, *et al.*, Eur. Phys. J. A **54**, 9 (2018).

[19] P. Talou, I. Stetcu, P. Jaffke, M. E. Rising, A. E. Lovell, and T. Kawano, Comput. Phys. Commun. **269**, 108087 (2021).

[20] G. C. Tyrrell, Nucl. Instrum. Methods A **546**, 180 (2005).

[21] `https://scintacor.com/products/6-lithium-glass`.

[22] `https://www.hamamatsu.com`.

[23] `https://eljentechnology.com/products/liquid-scintillators/ej-301-ej-309`.

[24] `https://www.caen.it/products/sy4527` (2020).

[25] `https://www.caen.it/products/v1730` (2020).

[26] `https://midas.triumf.ca`.

[27] S. Ritt, P. Amaudruz, and K. Olchanski, Proc. IEEE 10th Real Time Conf. , 309 (1997).

[28] K. J. Kelly, J. M. O'Donnell, D. Neudecker, M. Devlin, and J. A. Gomez, Nucl. Instrum. and Methods A **943**, 162449 (2019).

[29] A. D. Carlson, V. G. Pronyaev, R. Capote, G. M. Hale, Z.-P. Chen, *et al.*, Nucl. Data Sheets **148**, 143 (2018).

[30] G. Knoll, *Radiation Detection and Measurements* (John Wiley and Sons, 1996).

[31] K. J. Kelly, J. M. O'Donnell, M. Devlin, E. A. Bennett, and J. A. Gomez, Nucl. Instrum. Methods A , In Prep. (2022).

[32] K. J. Kelly, M. Devlin, J. M. O'Donnell, D. Neudecker, and E. A. Bennett, Nucl. Instrum. Methods A **1010**, 165552 (2021).

[33] B. E. Watt, Phys. Rev. **87**, 1037 (1952).

[34] J. Terrell, Phys. Rev. **113**, 527 (1958).

[35] H. Y. Lee, T. N. Taddeucci, R. C. Haight, T. A. Bredeweg, A. Chyzh, *et al.*, Nucl. Instrum. and Methods A **703**, 213 (2013).

[36] T. N. Taddeucci, R. C. Haight, H. Y. Lee, D. Neudecker, J. M. O'Donnell, *et al.*, Nucl. Data Sheets **123**, 135 (2015).

[37] K. J. Kelly, J. A. Gomez, J. M. O'Donnell, M. Devlin, R. C. Haight, *et al.*, Nucl. Instrum. and Methods A **954**, 161411 (2020).

[38] M. Devlin, J. A. Gomez, K. J. Kelly, R. C. Haight, J. M. O'Donnell, *et al.*, Nucl. Data Sheets **148**, 322 (2018).

[39] K. J. Kelly, T. Kawano, J. M. O'Donnell, J. A. Gomez, M. Devlin, *et al.*, Phys. Rev. Lett. **122**, 072503 (2019).

[40] D. Neudecker, R. Capote, D. L. Smith, and T. Burr, Nucl. Sci. Eng. **179**, 381 (2015).

[41] M. Sugimoto, A. B. Smith, and T. Guenther, Nucl. Sci. Eng. **97**, 235 (1987).

[42] A. J. Plompen, O. Cabellos, C. De Saint Jean, M. Fleming, A. Algora, *et al.*, Eur. Phys. J. **56**, 181 (2020).

[43] K. Shibata, O. Iwamoto, T. Nakagawa, N. Iwamoto, A. Ichihara, *et al.*, J. Nucl. Sci. Technol. **48**, 1 (2011).

[44] A. E. Lovell, P. Talou, I. Stetcu, and K. J. Kelly, Phys. Rev. C **102**, 024621 (2020).